

REYNOLDS NUMBER SCALING EFFECTS IN TRANSONIC CAVITY AERODYNAMICS: A HIGH-FIDELITY EXPERIMENTAL AND NUMERICAL FRAMEWORK

Andreas Goerttler[1], Stefan Koch[1], Michael Werner[1], Francesco Tocci[1], Florian Mayer[2] & Alexander Wagner[1]

[1]German Aerospace Center (DLR), Institute of Aerodynamics and Flow Technology, Department of High Speed Configurations, Bunsenstraße 10, 37073 Göttingen, Germany, Andreas.Goerttler@dlr.de
[2]Airbus Defence and Space GmbH, Rechliner Straße, 85077 Manching, Germany

Abstract

This paper outlines a comprehensive investigation designed to isolate and quantify the non-linear effects of Reynolds number on transonic cavity flows. Current semi-empirical prediction models often rely on low Reynolds number wind-tunnel data, which may not accurately represent the shear-layer dynamics and acoustic loading encountered at flight conditions. This study proposes a combined approach utilizing the Cryogenic Ludwieg-Tube in Göttingen (KRG) to independently vary Reynolds number while maintaining constant Mach number, together with high-fidelity numerical simulations. The methodology aims to determine how boundary-layer scaling influences the frequency of Rossiter modes, bridging the gap between sub-scale testing and full-scale operating conditions.

Keywords: Cavity Flow, Reynolds Number Effects, Aeroacoustics, Cryogenic Testing, Scaling Laws

1. Introduction

The internal carriage of stores in weapon bays is a defining feature of modern stealth aircraft, providing substantial reductions in radar cross-section and aerodynamic drag. However, the flow over these open cavities generates intense aeroacoustic loads driven by a self-sustained aeroacoustic feedback loop between shear-layer instabilities and acoustic wave propagation. As foundational research by Rossiter [1] and Charwat et al. [2] established, this process initiates when the incoming boundary layer separates at the cavity leading edge, forming an unstable free shear layer. Rockwell & Naudascher [3] reviewed these self-sustained oscillations and described how Kelvin-Helmholtz instabilities grow into vortical structures that convect downstream and impinge upon the aft wall. This impingement generates pressure perturbations that propagate upstream as acoustic waves, which in turn modulate the leading-edge separation, closing the loop and producing distinct resonant tones known as Rossiter modes.

A fundamental challenge in characterizing these flows is Reynolds-number scaling, since most wind-tunnel data are acquired at Reynolds numbers (Re) below those relevant to full-scale flight. While the Mach number (M) primarily drives compressibility effects and resonant frequencies, as modeled by the modified Rossiter-Heller equation [4], the Reynolds number governs viscous effects and the state of the incoming boundary layer. Early investigations into pressure distributions at supersonic speeds by Stallings & Wilcox [5] and at subsonic speeds by Plentovich et al. [6] established the baseline for flow regime identification. Research by Ahuja & Mendoza [7] demonstrated that the stability of the free shear layer is highly sensitive to the initial boundary layer momentum thickness (θ). At low Reynolds numbers, a thick boundary layer stabilizes the shear layer and reduces tonal amplitudes, whereas at flight-relevant high Reynolds numbers, the boundary layer is thinner. Recent cryogenic aeroacoustic

https://doi.org/10.71945/icas2026_0362

measurements by Ahlefeldt et al. [8] showed that Reynolds-number effects on aeroacoustic emission are nonlinear and become less pronounced with increasing Reynolds number.
The Cryogenic Ludwieg-Tube Göttingen (KRG), as detailed by Koch et al. [9], provides a unique operational envelope to isolate these viscous effects from compressibility. Characterization studies in the Langley Transonic Cryogenic Tunnel by Tracy & Plentovich [10] emphasize the value of such facilities in bridging the gap between sub-scale testing and operational flight. The complexity is further increased by three-dimensional (3D) features. Experimental work by Tracy et al. [11] showed that sweeping the leading edge produces streamwise vortices that can suppress the feedback loop, often preventing longitudinal resonance entirely. Similarly, operating at non-zero sideslip or yaw angles induces asymmetric vortex shedding. Research by Lee et al. [12] and Rajkumar et al. [13] indicates that such asymmetry can alter the dominant spectral content, including mode switching or mode splitting. Furthermore, Bacci and Saddington [14] found that the aircraft angle of attack significantly influences both mean-flow features and the induced structural loads on bay doors.
Practical weapon-bay configurations also involve interference between the cavity flow and internal stores. The interaction between stores and the cavity flow field, studied extensively by Stallings et al. [15] and Tracy & Plentovich [16], manifests as large-amplitude load fluctuations. Numerical studies by Kim et al. [17] and Barone & Arunajatesan [18] highlight the challenge of ensuring safe store separation given these repeatable sign-alternating forces. While Ben-Gida [19] observed that store presence might slightly reduce floor pressure fluctuations, the complex three-dimensional interaction remains a critical structural concern.
To resolve these dynamics, high-fidelity computational fluid dynamics (CFD) are required, as reviewed by Lawson & Barakos [20]. While Large Eddy Simulations are accurate, their cost necessitates hybrid approaches and strict adherence to scale-resolving best practices, such as those defined by Menter [21]. Recent comparative analyses by Bacci et al. [22] benchmarked traditional hybrid RANS/LES solvers against emerging Lattice-Boltzmann Method (LBM/VLES) frameworks. While both approaches provide accuracy within ± 10 dB, solvers often underpredict peak pitching moments. Future modelling efforts may leverage Gene Expression Programming (GEP), as introduced by Ferreira [23], to derive generalized prediction models that account for these complex 3D boundary-layer parameters and scaling laws.
To address these complexities, the primary objective of the present study is to establish a high-fidelity experimental and numerical framework capable of isolating viscous boundary-layer scaling from compressibility effects up to flight-relevant conditions of $250 \times 10^6\,\mathrm{m}^{-1}$. As a critical validation of this framework, the present paper evaluates the initial transonic dataset of this campaign, characterizing Rossiter mode sensitivities across a unit Reynolds number range of $30 \times 10^6\,\mathrm{m}^{-1} < Re_1 < 100 \times 10^6\,\mathrm{m}^{-1}$ at transonic Mach numbers.

2. Experimental Setup

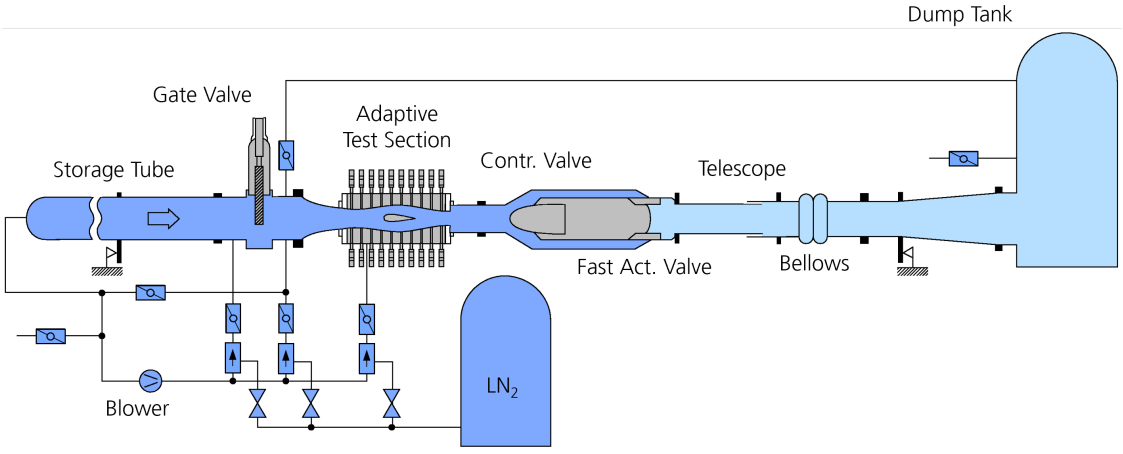


Figure 1 – Cryogenic Ludwieg-Tube Göttingen (KRG) at the German Aerospace Center (DLR)

To study Reynolds number effects rigorously, it is insufficient to simply increase velocity, as this

simultaneously alters the Mach number. Consequently, the experiment requires a facility in which density and viscosity can be varied through pressure and temperature while the Mach number is held fixed. The experiments are therefore conducted in the Cryogenic Ludwieg-Tube Göttingen (KRG), shown in Fig. 1, which operates with nitrogen gas at stagnation temperatures down to $120\,\mathrm{K}$ and stagnation pressures up to 10 bar [9]. This yields unit Reynolds numbers of up to $500 \times 10^6\,\mathrm{m}^{-1}$, a unique operational envelope that enables Reynolds number sweeps at a fixed transonic Mach number (e.g., $M = 0.7$). By lowering the temperature, which reduces the viscosity μ, and increasing the pressure, which increases the density ρ, the Reynolds number can be increased while maintaining fixed nominal Mach number.

The model consists of a flat plate with a clean rectangular cavity whose length-to-height ratio (L/H) can be varied between 5 and 12 to investigate both open and transitional cavity flow regimes, see Figs. 2 and 3. The assembly can be rotated by up to 10° to investigate sideslip (β) effects, which can induce asymmetric shear-layer development and alter the effective feedback length, thereby modifying the resonant frequency [13].

The cavity geometry is based on the DLR Generic Cavity Model, a benchmark configuration used in the international Weapons Bay Store Separation Workshop (WBS^{2}W) to enable cross-validation of CFD methods. The cavity length $L = 215\,\mathrm{mm}$ and width $W = 67\,\mathrm{mm}$ are fixed, while the cavity height H is varied to obtain length-to-height ratios L/H from 5 to 12, with corresponding W/H ratios between 1.56 and 3.74. The cavity dimensions are summarized in Table 1, which defines the physical dimensions of the test cases.

Table 1 – DLR Generic Cavity Model dimensions used in the Weapons Bay Store Separation Workshop (WBS^{2}W). This geometry serves as a benchmark for transonic cavity flow studies.

H (mm)	L/H	W/H
43.00	5	1.56
35.83	6	1.87
30.71	7	2.18
26.88	8	2.49
21.50	10	3.12
17.92	12	3.74

A photograph of the actual experimental hardware prior to wind-tunnel installation is provided in Figure 7, illustrating the clean surface finish of the flat plate and the modular cavity insert region. The test section is equipped with two possible configurations of the flat plate: a long setup with the cavity leading edge located at $x = 0.7215\,\mathrm{m}$ from the flat plates leading edge and a shorter setup with the cavity leading edge at $x = 0.4715\,\mathrm{m}$, enabling the investigation of boundary layer thickness effects in a wide range, together with the boundary layer thickness adjustment via the wind tunnel Reynolds number. The Reynolds number is defined based on this reference length x, with $Re_x = \rho U x/\mu$. This allows for consistent comparison across setups and ensures that the boundary layer state is well-characterized at the cavity entrance.

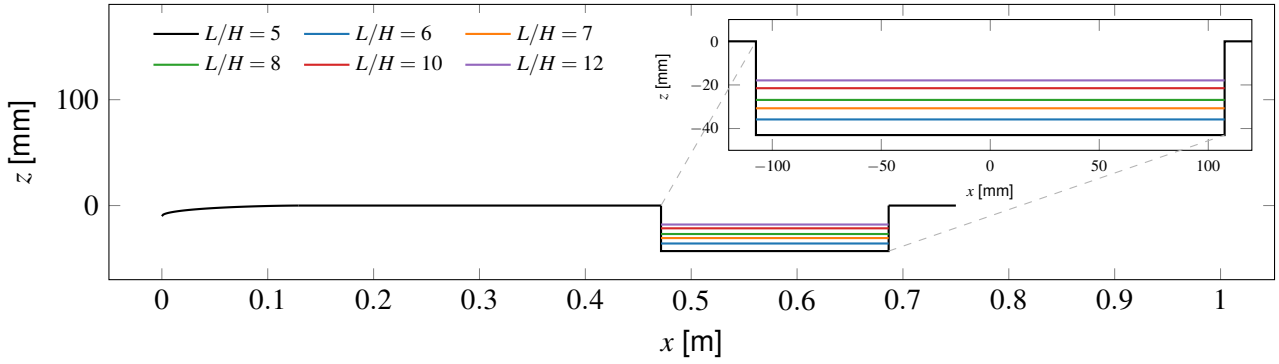


Figure 2 – Dimensions of cavity for different L/H ratios with short plate setup.

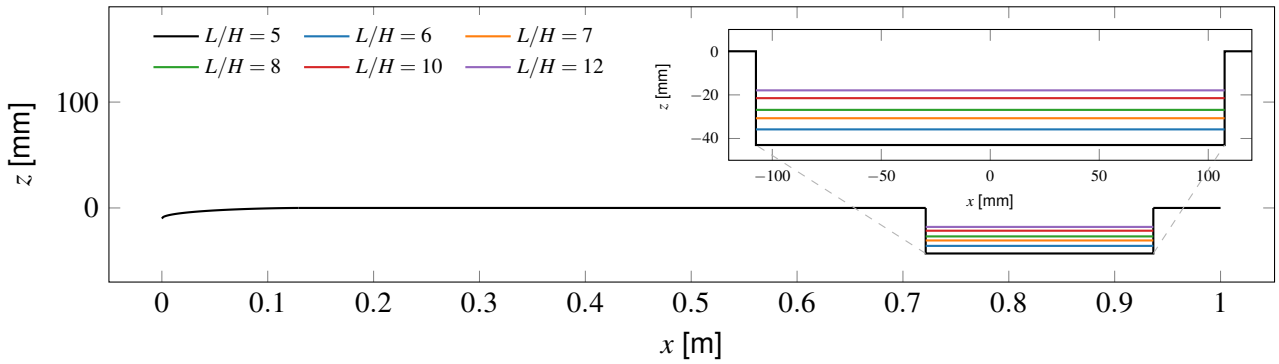


Figure 3 – Dimensions of cavity for different L/H ratios with long plate setup.

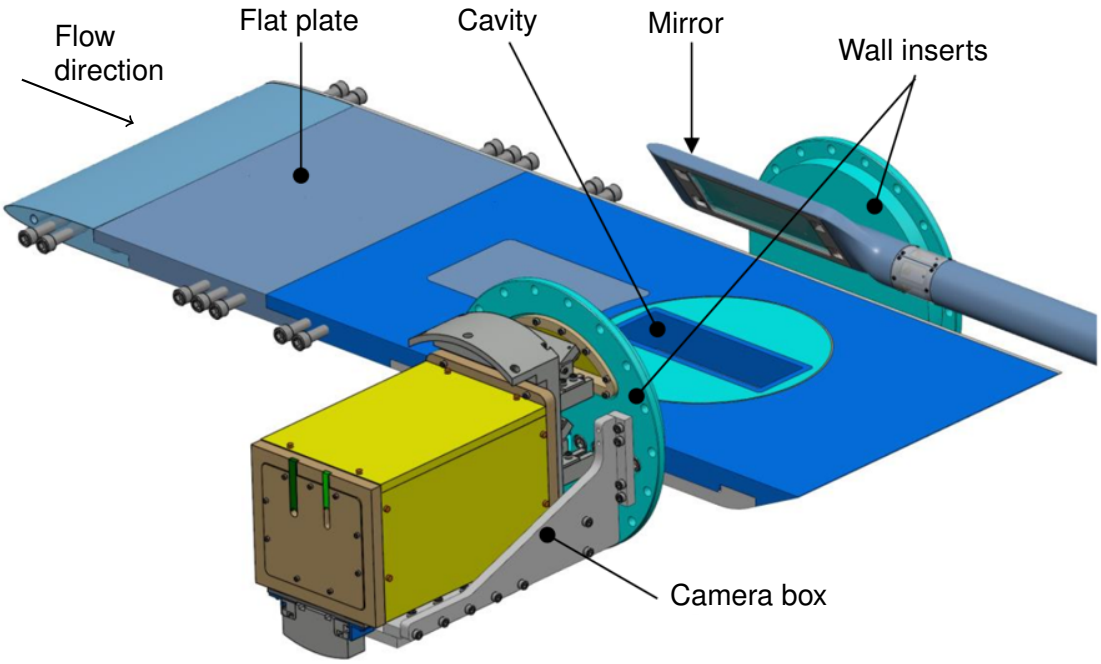


Figure 4 – CAD representation of the long flat plate with cavity and optical system.

3. Sensor Configuration and Instrumentation

To comprehensively capture the unsteady pressure dynamics within the cavity and along its walls, a combined instrumentation approach is employed. The experimental setup integrates both pointwise dynamic pressure measurements and full-field surface pressure mapping to resolve the complex feedback mechanisms governing cavity aeroacoustics.

The primary dynamic measurement system consists of seven piezoresistive pressure sensors (Kulite CCQ series), installed at selected streamwise locations along the cavity floor, side walls, and aft wall. Depending on the selected cavity height, the side-wall sensors can be installed at two different heights. These sensors measure high-frequency pressure fluctuations up to $100\,\mathrm{kHz}$, enabling characterization of shear-layer instabilities and the temporal evolution of Rossiter modes. The sensor positions are concentrated in the downstream half to capture the spatial development of the feedback loop.

In addition to the dynamic sensors, a cryogenic pressure-sensitive paint (iPSP) system is installed to provide full-field, time-resolved surface-pressure data during the wind-tunnel campaign. This optical technique relates the local pressure to the luminescence response of the paint, allowing for spatially resolved pressure mapping across the cavity floor and one side wall. A mirror mounted above the cavity provides optical access for the camera system (see Figs. 4). While the experimental model is configured to accommodate a cryogenic iPSP system for future full-field surface pressure mapping, the present study is restricted to the localized high-frequency analysis obtained from the dynamic

Kulite sensors.
Figure 5 shows the full static-pressure layout in the long setup configuration, while Fig. 6 provides a zoomed view of the cavity region, including the Kulite dynamic-pressure sensors (red markers) and the static pressure taps (blue markers). The Kulite sensors provide the pressure time histories used for the frequency analysis presented below, while the iPSP system is retained as part of the broader measurement campaign and will provide complementary full-field pressure information for future comparison with the numerical simulations.

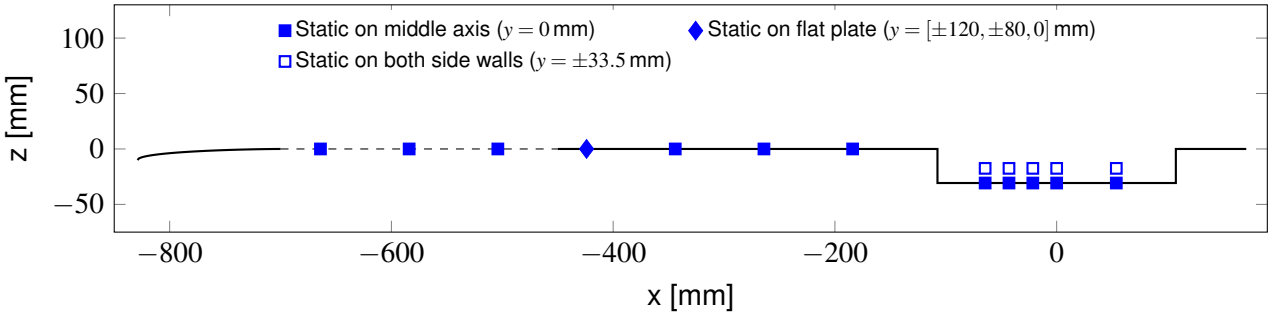


Figure 5 – Full-scale spatial distribution of static pressure taps.

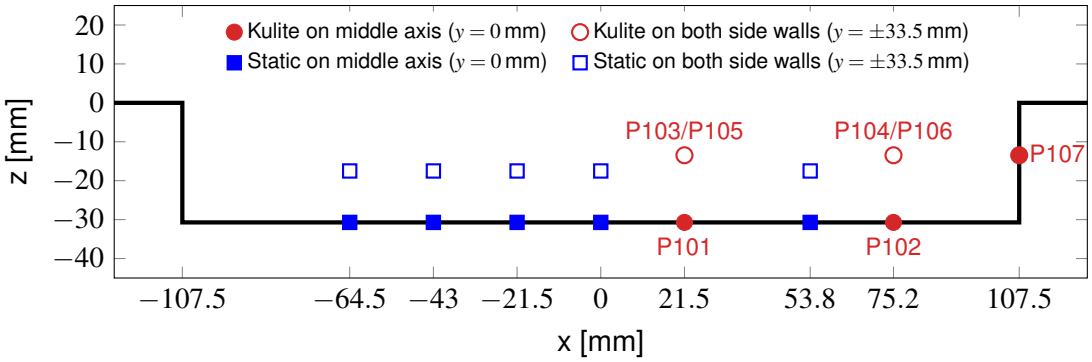


Figure 6 – Detailed sensor placement inside the cavity area.

4. Numerical Methodology

The numerical simulations presented in this paper were performed using the DLR TAU code [25]. The TAU code is a flow solver for the solution of the Reynolds-averaged Navier-Stokes equations based on the finite volume approach and developed by the German Aerospace Center (DLR). It is widely used in academia and industry in Germany and Europe. It offers a wide range of numerical schemes and approaches to turbulence modelling, including several hybrid RANS-LES methods. To capture the complex flow topology developing in the cavity at high Reynolds numbers, the current



Figure 7 – Model of flat plate with cavity

simulations use an improved delayed detached eddy simulation (IDDES) approach, based on the two-equation Menter Shear Stress Transport model [26], together with a low-dissipation, low-dispersion scheme [27]. The spatial discretisation uses a second-order central scheme for the convective mean-flow fluxes, together with a first-order Roe scheme for the turbulent fluxes. For the temporal integration, a second-order dual-time stepping approach is used, with an implicit backward-Euler scheme for the solution of the resulting linear system. The time-step size is set to $2.5 \times 10^{-6}\,\mathrm{s}$ for all cases. To assess the convergence of the inner iterations of each physical time step, a Cauchy convergence criterion is used, where convergence of the inner iterations is assumed if the relative change of selected monitor variables remains below 5×10^{-6} over the last 30 inner iterations. For the setup of the boundary conditions, a simplified approach was chosen. Specifically, the wind tunnel is not explicitly modelled, avoiding the need to adapt the upper and lower wall contours to obtain the target Mach number. Instead, the side walls of the wind tunnel are treated as inviscid walls, and the upper and lower test-section walls are replaced with a virtual farfield to avoid blockage effects. The size of the farfield is $\pm 50\,\mathrm{m}$ in x-direction and $\pm 10\,\mathrm{m}$ in z-direction. To ensure this geometric simplification does not introduce errors, the numerical freestream conditions for each case were specifically chosen to match the exact local Mach number measured immediately upstream of the cavity leading edge in the physical facility. By calibrating the computational inflow to this local target rather than the nominal tunnel setting, this computational approach directly compensates for any unmodelled blockage or wall interference, ensuring a high-fidelity representation of the actual shear layer development. The plate and cavity are modelled as fully turbulent viscous walls.

4.1 Mesh Generation

The computational mesh is generated using the commercial meshing software ANSA [28]. The mesh uses a hybrid unstructured topology, with a quasi-structured near-wall mesh to better resolve the boundary layer and a hexahedra-dominant unstructured volume mesh in the rest of the computational domain. The maximum cell size of the surface mesh on the plate is $5\,\mathrm{mm}$, and is further reduced to $2\,\mathrm{mm}$ in the immediate surroundings of the cavity. To better capture the shear-layer instabilities near the leading edge of the cavity, the maximum cell size along the leading edge of the cavity is reduced further to $1\,\mathrm{mm}$. The volume-cell sizes are matched to the corresponding surface-cell sizes in the refined regions. Finally, to better resolve the boundary layer along the viscous walls, the near-wall flow field is meshed using a quasi-structured layer mesh. The height of the first cell is chosen such that a dimensionless wall distance of $y^+ \approx 1$ is achieved for all investigated cases. This results in a first-cell height of $3 \times 10^{-4}\,\mathrm{mm}$. The boundary layer mesh then consists of 55 layers with a growth rate of 1.175, resulting in a total height of about $12\,\mathrm{mm}$. The resulting volume mesh around the cavity is shown on the model symmetry plane in Fig. 8.

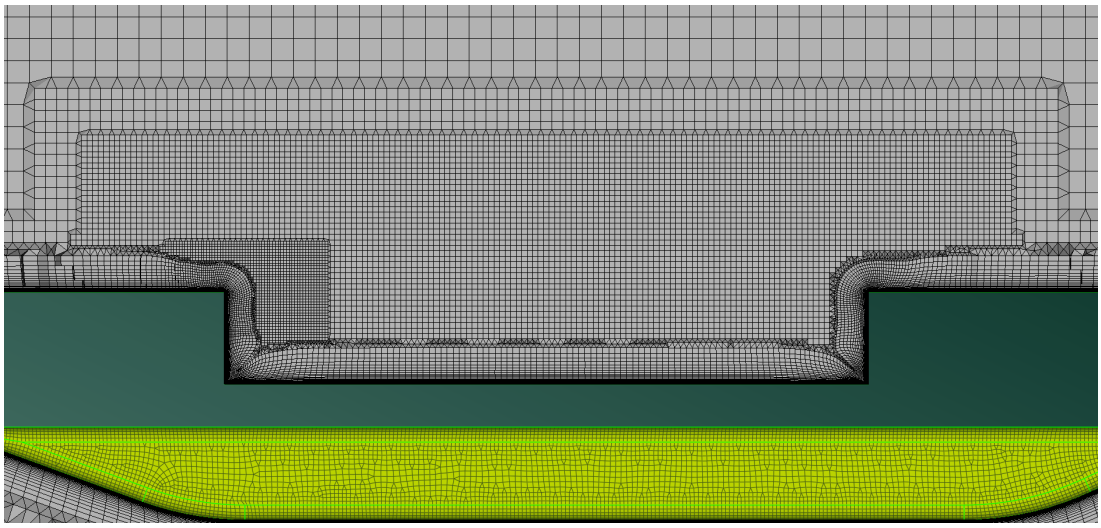


Figure 8 – Depiction of the volume mesh around the cavity on the xz-symmetry plane, including the refinement region near the leading edge of the cavity.

4.2 Simulation Procedure

To balance computational efficiency with scale-resolving accuracy, a dual-stage temporal strategy is implemented for the numerical campaign. The flow field is initially advanced using an unsteady Reynolds-Averaged Navier-Stokes (URANS) approach for $0.1\,\mathrm{s}$ to eliminate transient startup effects and establish a mature flow topology. This is followed by a $0.06\,\mathrm{s}$ Improved Delayed Detached Eddy Simulation (IDDES) run. For subsequent statistical and spectral analysis, only the final $0.05\,\mathrm{s}$ of the IDDES time-history is extracted, which corresponds to approximately 50 convective time units based on the cavity length and freestream velocity.

Spectral estimation of the unsteady pressure signals is performed using Welch's method configured with a Hanning window. Using the full simulated sampling duration of approximately $0.05\,\mathrm{s}$ would yield a nominal frequency-bin spacing of $20\,\mathrm{Hz}$. However, estimating the spectrum from a single undivided segment leads to a high-variance spectral estimate because of the limited sampling duration.

To obtain smoother, statistically stable signals, a sub-windowing strategy with 50% overlap is implemented where the time-history is divided into segments of half the total duration and subsequently averaged. Although this averaging approach coarsens the effective frequency-bin spacing to approximately $40\,\mathrm{Hz}$, it reduces the variance of the spectral estimate and makes the dominant resonant tones more clearly identifiable.

By contrast, the physical experimental facility allows for a significantly longer data acquisition window of $0.4\,\mathrm{s}$, enabling a finer spectral resolution of $2.5\,\mathrm{Hz}$ for direct comparison with the analytical Rossiter-Heller mode. To mitigate this resolution mismatch during direct comparison, the longer experimental time-history is processed using an identical sub-windowing and averaging constraint, matching both datasets to an identical frequency resolution.

Because the scale-resolving IDDES solver captures a rich, highly dynamic multi-modal environment, the numerical spectra contain multiple spectral peaks. To ensure a consistent comparative analysis across the Reynolds sweep, the first three dominant peaks were systematically extracted from the numerical data at each probe location, and the specific peak situated closest to the analytical second Rossiter mode was selected for tracking.

5. Experimental Parameters and Test Matrix

To isolate the effects of Reynolds number on transonic cavity aeroacoustics, a carefully designed test matrix is employed at a fixed Mach number of $M = 0.90$. This transonic condition is defined by the static pressure measured at the last pressure sensor located just upstream of the cavity leading edge, which corresponds to the expected static pressure for $M = 0.90$ under isentropic flow assumptions. This ensures that compressibility effects, such as shock wave formation and wave-boundary layer interactions, are held constant across all test cases, enabling a clean separation of viscous (Reynolds number) effects.

The unit Reynolds number is varied over a wide range, spanning from approximately $30 \times 10^6\,\mathrm{m}^{-1}$ to $100 \times 10^6\,\mathrm{m}^{-1}$. This is achieved using the cryogenic capabilities of the KRG facility, where the Reynolds number is independently increased by adjusting the stagnation pressure (p_0) and stagnation temperature (T_0) of the incoming flow, while maintaining constant Mach number. The unit Reynolds number is defined as: $Re_1 = \rho U l/\mu$ where U is the velocity, ρ is the fluid density, μ is the dynamic viscosity and l is set to $1m$. The local Reynolds number is based on the streamwise distance x from the plate leading edge to the cavity leading edge, which is either $x = 0.7215\,\mathrm{m}$ (long setup) or $x = 0.4715\,\mathrm{m}$ (short setup), depending on the test configuration. For the current study, the long plate configuration ($x = 0.7215\,\mathrm{m}$) is utilized exclusively to establish the baseline dataset, while the short plate configuration is reserved for future investigations.

In particular, two distinct test conditions are established at $Re_1 \approx 75 \times 10^6\,\mathrm{m}^{-1}$ to investigate the influence of the thermodynamic state on flow physics. Crucially, the stagnation temperature T_0 differs significantly between these two cases: Case B3.b ($T_0 = 272.7\,\mathrm{K}$) and Case B3.c ($T_0 = 211.0\,\mathrm{K}$). Since the freestream speed of sound is $c = \sqrt{\kappa R T_\infty}$ and, at fixed Mach number, T_∞ scales with T_0, the two stagnation-temperature levels result in different acoustic time scales, even though the Mach number is identical.

This has a profound implication for the aeroacoustic feedback loop: the time it takes for an acoustic

wave to travel from the cavity aft wall back to the leading edge (the feedback delay) is inversely proportional to the speed of sound. Therefore, a lower T_0 reduces both the freestream speed of sound and, at fixed Mach number, the freestream velocity. This increases the dimensional acoustic and convective time scales, shifting the Rossiter-mode frequencies to lower values.
This unique experimental design enables a decoupled study of Reynolds number, which governs boundary-layer thickness and shear-layer dynamics, and of the speed of sound via T_0, which governs the acoustic time scale and thus the feedback frequency.
This allows investigation of whether the observed scaling of Rossiter mode amplitudes and frequencies is driven primarily by viscous effects, or whether the thermodynamic state, through its influence on the acoustic time scale, plays an equally critical role.
The test matrix of the 0.9 Mach cases is summarized in Table 2, which lists the unit Reynolds number, the Reynolds number (Re_x), stagnation pressure (p_0), and stagnation temperature (T_0) for each test condition.

Table 2 – Test matrix for Reynolds number variation at $M = 0.90$. All tests are conducted with the same cavity geometry ($L/H = 7$) and zero sideslip. The Reynolds number is based on the reference length $x = 0.7215\,\mathrm{m}$ from the test section leading edge to the cavity leading edge.

Case	Unit Reynolds No. Re_1 (m^-1)	Local Reynolds No. Re_x	Stagnation Pressure p_0 (Pa)	Stagnation Temperature T_0 (K)
B3.a	29.68×10^6	21.4×10^6	193,029.2	274.4598
B3.b	75.32×10^6	54.3×10^6	485,147.1	272.7351
B3.c	74.75×10^6	53.9×10^6	342,412.9	210.9763
B3.d	100.1×10^6	72.2×10^6	463,044.0	212.7399

These test conditions are designed to span the transition from model-scale to flight-relevant Reynolds numbers, capturing the onset of non-linear effects such as shear-layer stabilization, mode suppression, and potential saturation of acoustic loads—key phenomena observed in recent high-Re experiments [8]. The resulting high-fidelity dataset will serve as a benchmark for validating advanced CFD solvers and refining semi-empirical prediction models.
This experimental campaign is part of the international *Weapons Bay Store Separation Workshop*, a collaborative effort aimed at advancing the understanding and predictive capability of cavity flows in weapon bay environments. The workshop, hosted on GitHub at https://github.com/Weapons-Bay-Store-Separation-Workshop, brings together researchers from academia, industry, and national laboratories to share high-fidelity data, validate numerical models, and develop standardized benchmark cases for transonic cavity flows. The present study contributes to this initiative by providing a well-documented, Reynolds number-resolved dataset at $M = 0.90$, which will be made publicly available through the workshop's repository to support future CFD validation and scaling studies.

6. Results

The experimental measurements and high-fidelity numerical simulations yield a consistent and robust frequency response across the internal geometry of the cavity. Across all evaluated experimental test cases, spanning from the baseline condition to the highest Reynolds number sweeps, the array of seven piezoresistive dynamic pressure sensors successfully identified a uniform dominant resonant frequency footprint. This unified spectral signature indicates a highly synchronized aeroacoustic state inside the physical boundaries of the cavity model, reflecting a clean coupling within the self-sustained aeroacoustic feedback loop. To establish a baseline for the global behaviour of these oscillations before evaluating localized flow topologies, the unsteady pressure fluctuations must be characterized in both the temporal and frequency domains.

6.1 Experimental results

The primary characteristics of this synchronized resonance are highlighted in Figure 9, which depicts the raw unsteady pressure time-history alongside its corresponding Sound Pressure Level (SPL) spectrum extracted from probe P102 at the rear cavity floor for $M = 0.90$ and $Re = 100.1 \times 10^6$. The

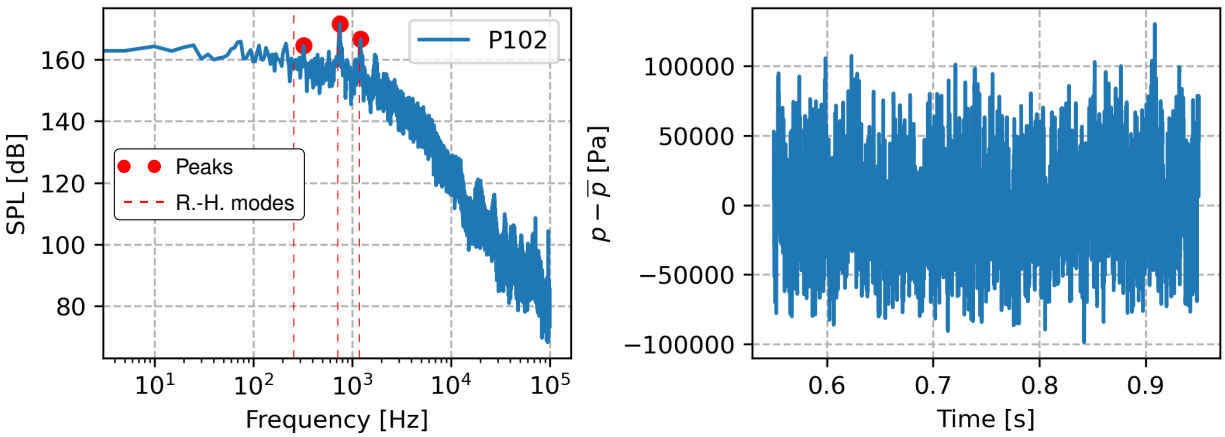


Figure 9 – Unsteady pressure time-history (right) and corresponding sound pressure level spectrum (left) extracted from probe P102 at the rear cavity floor for $M = 0.90$ and $Re = 100.1 \times 10^6$.

vertical dashed lines are the first three Rossiter-Heller modes. As seen in the time-domain signal, the cavity flow field experiences intense, repeatable pressure fluctuations that fluctuate sharply between large positive and negative limits of approximately $\pm 100\,000\,\mathrm{Pa}$. When transformed into the frequency domain, this high-frequency pressure dynamic resolves into a high-amplitude peak above $170\,\mathrm{dB}$, standing several orders of magnitude above the broadband turbulent background noise. This dominant peak (marked by a red dot) indicates the principal resonant frequency of the system, matching well with the theoretical second Rossiter-Heller mode denoted by the second vertical dashed line. The secondary, lower-amplitude spikes visible at surrounding frequencies confirm the presence of higher-order modes close to the Rossiter-Heller modes.

The analysis of the pressure data shows a consistent frequency response across the cavity. In all experimental test cases (B3.a through B3.d), the array of seven Kulite dynamic pressure sensors (P101–P107) capture a closely matching dominant frequency. Figure 10 compares the experimental results with theoretical predictions from the modified Rossiter-Heller equation.

The modified Rossiter-Heller equation is given by:

$$f = \frac{v}{L}\left(\frac{m - 0.062\frac{L}{H}}{\frac{1}{k_v} + \frac{Ma}{\sqrt{1+\frac{\gamma-1}{2}Ma^2}}}\right)$$

For the baseline case (Case B3.a), the measured experimental frequency of 870 Hz is in relatable agreement with the Rossiter-Heller prediction of 790.7 Hz. A notable frequency reduction is observed in the transition to the cold flow condition (Case B3.c). This shift is consistent with the lower speed of sound and freestream velocity at a reduced stagnation temperature, both of which scale approximately with $\sqrt{T_0}$ at a fixed Mach number.

A much weaker Reynolds number dependence is observed within each isolated temperature group. Higher Reynolds numbers lead to a subtle decrease in frequency, a physical nuance that standard Rossiter-Heller formulations do not fully capture.

To isolate whether these frequency shifts are driven by structural changes in the cavity mode physics or are merely a consequence of the fluid's thermodynamic state, the non-dimensional Strouhal number $Sr = fL/U$ must be analyzed. While the theoretical Strouhal number for the second Rossiter mode remains entirely unchanged at 0.605, the experimental values remain closely aligned across the temperature groups. Specifically, the experimental Strouhal number shifts slightly from 0.656 for the normal condition (Case B3.b) to 0.66 for the cold condition (Case B3.c) at an identical unit Reynolds number. This close agreement demonstrates that the substantial drop in the dimensional resonant frequency, from $877.5\,Hz$ down to $757.5\,Hz$, is driven primarily by the scaling of the acoustic and convective time-scales via $\sqrt{T_0}$ rather than a structural reorganization of the flow.

To evaluate the global aeroacoustic behavior of the cavity across a broader operational envelope, a comprehensive Mach number sweep from $M = 0.4$ to $M = 0.9$ was analyzed. Figure 11 plots the

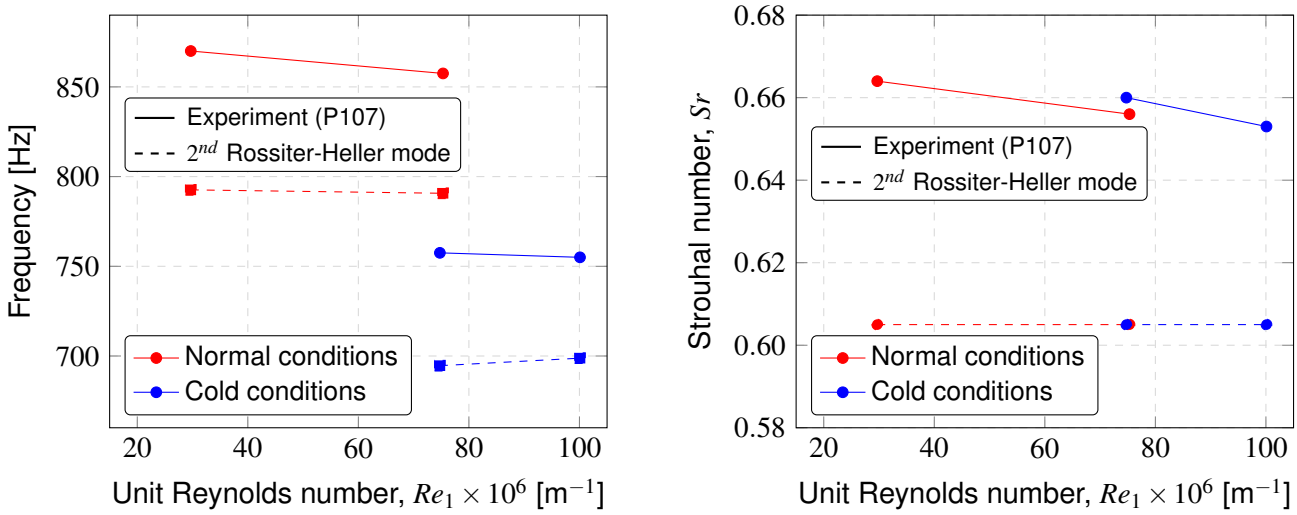


Figure 10 – Frequency and Strouhal number dependency on the Reynolds number for experimental data and for the analytical second Rossiter-Heller mode for the $M = 0.90$ cases.

resulting dimensional resonant frequencies for both the second and third Rossiter modes, alongside their respective analytical predictions across different unit Reynolds numbers and thermodynamic states.

The analytical curves illustrate a monotonic increase in resonant frequency as the Mach number rises. Crucially, these theoretical baselines highlight the dominant influence of the stagnation temperature: the warm configurations ($T_0 = 283K$) sit systematically higher in frequency than the cold configurations ($T_0 = 223K$). This clear vertical separation reflects the altered speed of sound and freestream velocity under cold conditions, confirming that the thermodynamic state dictates the primary acoustic and convective time scales of the feedback loop across the entire subsonic and transonic regimes.

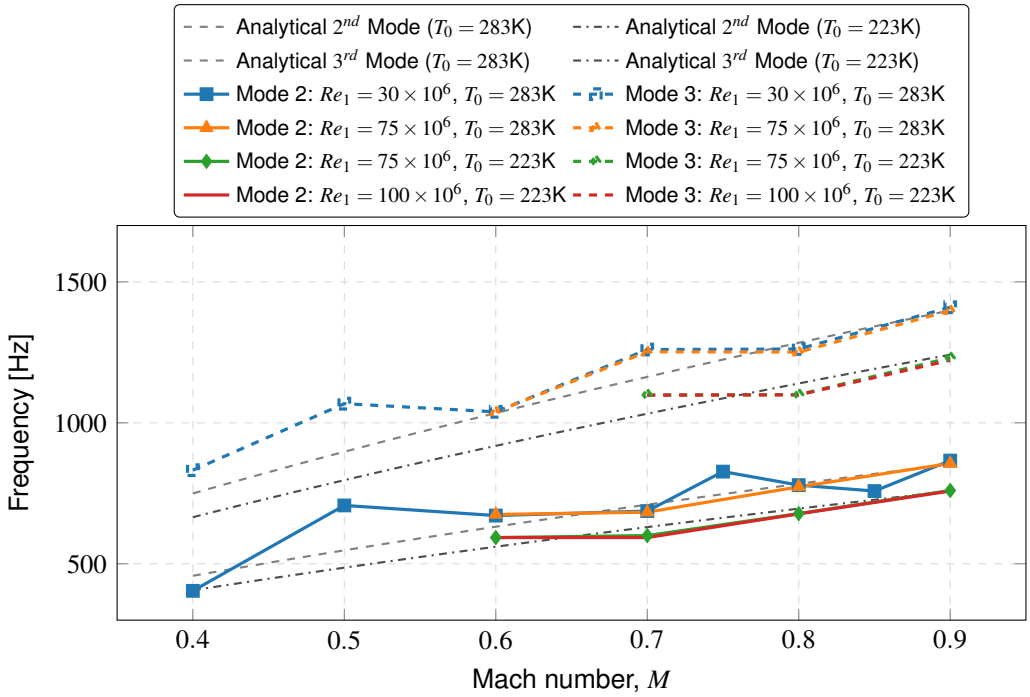


Figure 11 – Dominant aeroacoustic resonant frequencies tracked across a comprehensive Mach number sweep for different unit Reynolds numbers and thermodynamic states.

The tracked data points, systematically extracted from the multi-modal numerical spectra, exhibit

good agreement with these theoretical trends. The data cleanly divides into two distinct modal bands, where the Mode 2 tracks follow the lower analytical curves and the Mode 3 tracks align closely with the higher-frequency predictions. Within each isolated temperature group, the data points form highly coherent clusters. This highlights that while the macroscopic dimensional frequency is heavily driven by the baseline thermodynamic state, the subtle variations within each cluster contain the highly nuanced viscous scaling effects. This difference in scale underscores why separating the dominant thermodynamic parameters from the underlying Reynolds-number dependencies is a key requirement for isolating true boundary-layer scaling laws.

6.2 Comparison with CFD

To evaluate the predictive capability of the scale-resolving numerical setup, the computational results are benchmarked directly against the experimental wind-tunnel data. Figure 12 illustrates the numerical IDDES dimensional frequency results plotted against the unit Reynolds number Re_1. These data are systematically tracked for three distinct computational monitoring probes located within the cavity geometry, P101 and P102 positioned along the cavity floor, and P107 situated at the center of the vertical aft wall, and are evaluated alongside the experimental baseline data. To enable a direct comparison, the results are organized into side-by-side column groups across the four investigated operating conditions. Numerical IDDES predictions are distinguished by solid columns, while the corresponding wind-tunnel baseline measurements are depicted using color-matched, semi-transparent bars.

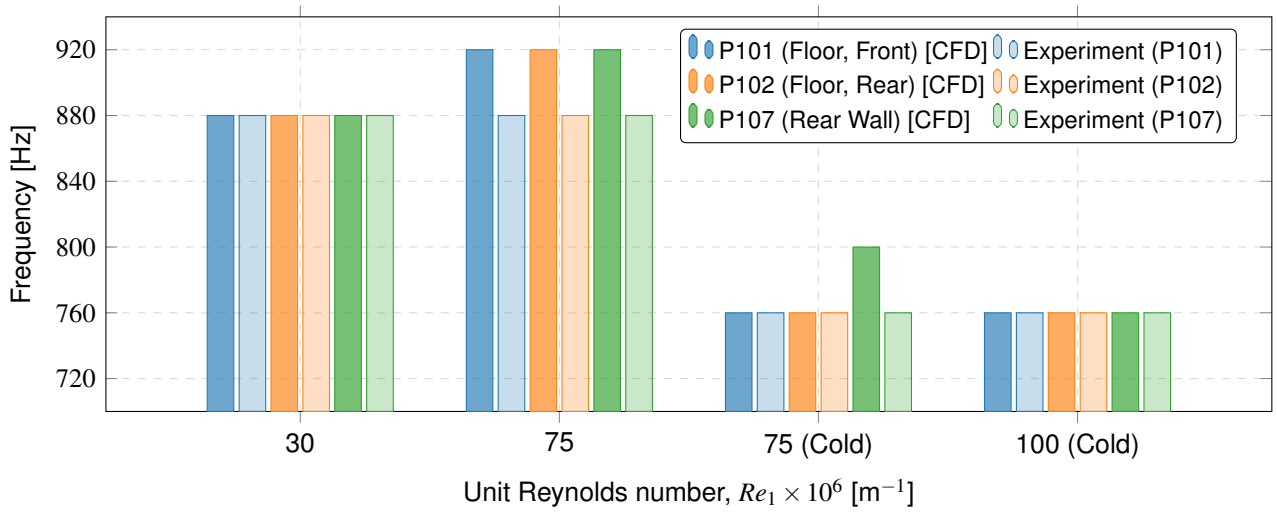


Figure 12 – Frequency dependency on the unit Reynolds number comparing scale-resolving IDDES probe configurations directly with physical baseline wind-tunnel data at Mach=0.90.

Both the numerical and windowed experimental time-histories are processed into identical frequency bins to ensure a consistent comparison. Because the signal processing utilizes a shared sub-windowing and averaging strategy, the final spectra are constrained to an effective frequency resolution of $40\,\mathrm{Hz}$. Within this discrete spectral environment, localized deltas across the column groups must be interpreted with respect to this underlying $40\,\mathrm{Hz}$ bin size. While an apparent numerical shift of exactly $40\,\mathrm{Hz}$ indicates that the tracked peak has mapped to an adjacent discrete bin, such variations can also point to minor physical sensitivities, such as slight differences in the simulated shear-layer convection velocity or the initial boundary layer profile upstream of the cavity.

The resulting clustered columns reveal a coherent and synchronized aeroacoustic environment across all investigated conditions. At the baseline case $Re_1 \approx 30 \times 10^6\,\mathrm{m}^{-1}$, all three numerical tracking probes align with the experimental baseline at $880\,\mathrm{Hz}$. As the unit Reynolds number increases within the normal temperature group $Re_1 \approx 75 \times 10^6\,\mathrm{m}^{-1}$, the three computational probes cluster at $920\,\mathrm{Hz}$, while the physical probe registers at $880\,\mathrm{Hz}$. This delta of exactly $40\,\mathrm{Hz}$ corresponds to a variance of just a single frequency bin, confirming that the solver reproduces the global feedback cycle with reasonable precision.

This high predictive fidelity is maintained when scaling into the cold configurations, where the reduction in the freestream speed of sound forces a drop in the dimensional resonant frequencies. For both the intermediate ($Re_1 \approx 75.5 \times 10^6\,\mathrm{m}^{-1}$) and the maximum ($Re_1 \approx 100.1 \times 10^6\,\mathrm{m}^{-1}$) Reynolds configurations, the computational floor sensors (P101 and P102) lock cleanly onto the physical baseline at 760 Hz. The slight upward deviation observed at the computational rear-wall probe (P107) under cold conditions similarly represents a single-bin discretization shift.

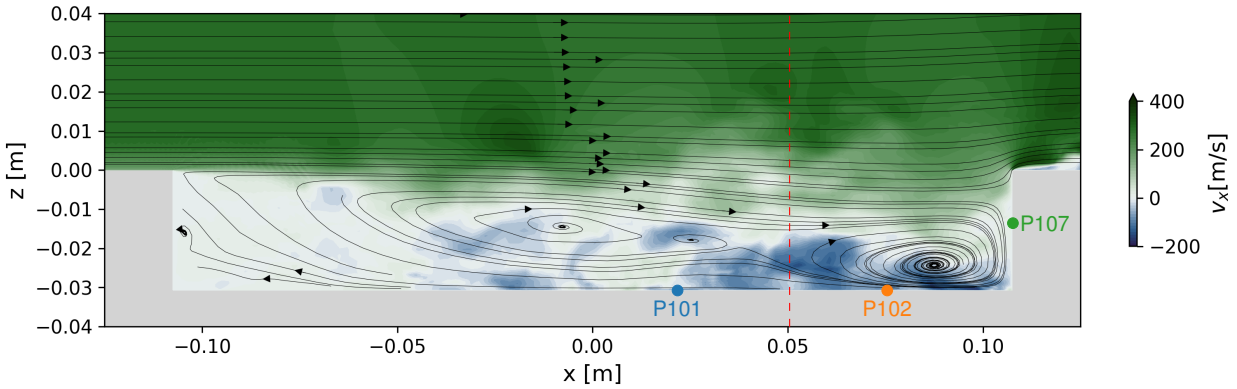


Figure 13 – Instantaneous x-velocity (v_x) contour and time-averaged streamlines in a centerline cut for the normal condition 75×10^6 Reynolds number case.

Visualizations of the flow field are provided in Figures 13 and 14. Figure 13 displays a centerline cut of the instantaneous x-velocity component for the normal $Re_1 = 75 \times 10^6$ case. The contour highlights the complexity of the shear layer, showing large regions of backward flow (negative v_x in blue) within the cavity. The overlaid time-averaged streamlines reveal two primary recirculation zones: a large clockwise vortex dominating the center and a secondary vortex near the aft wall. The locations of pressure probes P101, P102, and P107 are marked to show their positions relative to these high-gradient flow regions.

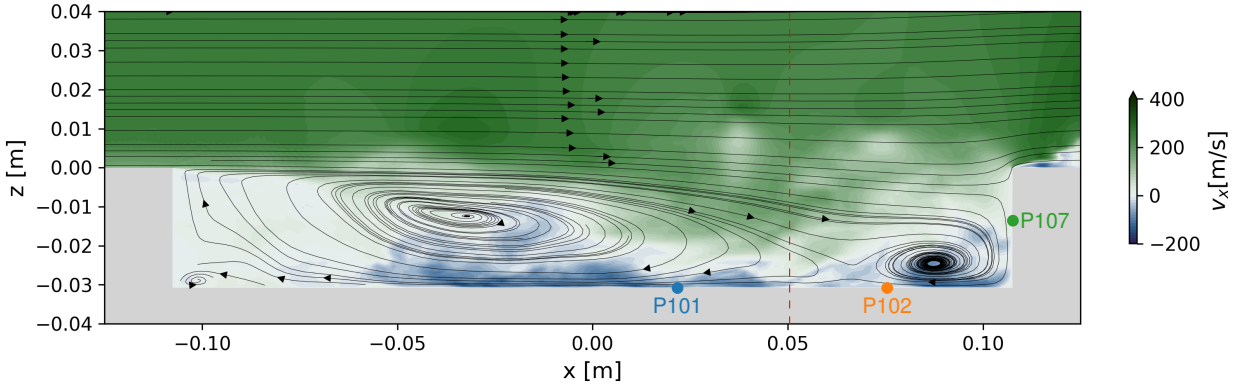
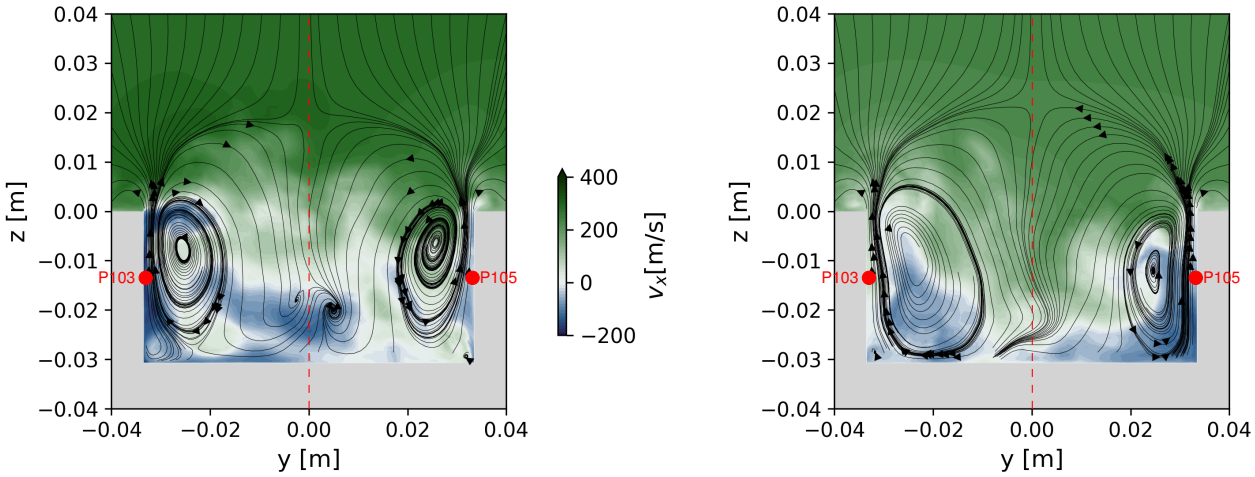


Figure 14 – Instantaneous x-velocity (v_x) contour and time-averaged streamlines in a centerline cut for the cold 75×10^6 Reynolds number case

Figure 14 shows the same setup under cold flow conditions (B3.c) at the same Reynolds number. While the general flow topology remains similar to the warm case, the instantaneous velocity fluctuations indicate a higher density of fine-scale structures. The averaged streamlines also exhibit minor differences in the shape and core location of the primary recirculation vortex, suggesting that the thermodynamic state of the gas influences not only the acoustic time scales but also the mean flow structure within the cavity.

The three-dimensional flow field driving these localized probe sensitivities is visualized in Figure 15, which illustrates the instantaneous spanwise velocity contours overlaid with time-averaged streamlines in a cross-sectional cut at $x = 0.05\,\mathrm{m}$ between the sensors. The comparison between the normal and cold flow states reveals a pair of highly energetic, counter-rotating streamwise vortices nested



(a) Normal condition at $Re_1 \approx 75x10^6$.

(b) Cold condition at $Re_1 \approx 75x10^6$.

Figure 15: Instantaneous x-velocity (v_x) contour and time-averaged streamlines in a spanwise cut at $x = 0.05\,m$.

symmetrically along the left and right side walls of the cavity structure. In the normal configuration, shown in Figure 15(a), these primary recirculation cores appear highly coherent and tightly contained near the side boundaries. Conversely, the cold condition in Figure 15(b) showcases a higher density of fine-scale turbulent structures and minor structural changes in the shape and core locations of the vortices. This visual discrepancy demonstrates that the gas's thermodynamic state exerts a dual influence on the cavity system, scaling not only the temporal acoustic feedback via the speed of sound, but also altering the underlying spatial mean flow and shear-layer development.

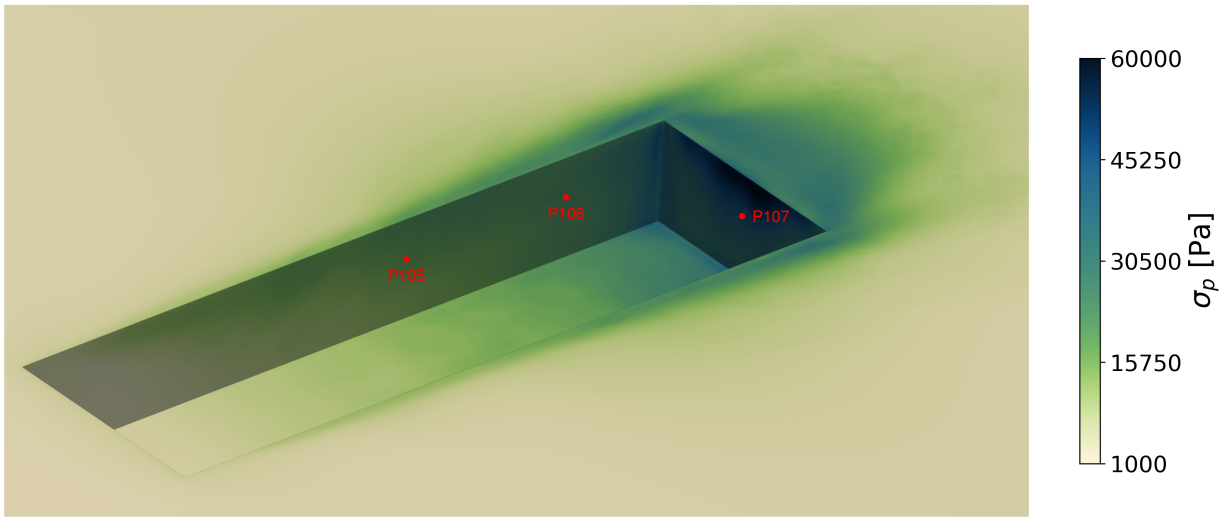


Figure 16 – Contours of computed surface pressure standard deviation (σ_p) across the cavity floor and walls for the $Re_1 = 100.1 \times 10^6$ m^{-1} Case B3.d.

To directly correlate these 3D flow topologies with the resulting aeroacoustic loading, the spatial distribution of the surface pressure standard deviation (σ_p) is evaluated in Figure 16. This Figure illustrates the computed surface footprint across the cavity floor and walls for the highest Reynolds number (Case B3.d, $Re_1 = 100.1 \times 10^6$ m^{-1}). The standard deviation serves as a direct metric for the local amplitude of the self-sustained pressure oscillations.

The footprint exhibits a highly symmetric distribution along the cavity centerline, indicating a well-balanced longitudinal resonance state free from sideslip-induced asymmetric vortex shedding. Near the leading edge, the fluctuations remain small ($\sigma_p \approx 1{,}000$ Pa), characteristic of the initial laminar-to-turbulent shear layer transition. Moving downstream, σ_p increases rapidly as the convective Kelvin-

Helmholtz instabilities grow into large-scale coherent structures.
The maximum acoustic loading is concentrated on the upper half of the aft wall and trailing edge lip, peaking near $60000\,\mathrm{Pa}$. This localized peak marks the violent impingement zone of the shear layer vortices against the vertical rear face, driving the upstream-traveling acoustic feedback loop. Additionally, distinct channels of elevated pressure fluctuations flank the outer lateral edges of the cavity floor; these track the path and footprint of the counter-rotating streamwise side vortices previously identified in the spanwise planes (see Fig. 15).
The sensor locations shown in Figure 16 provide additional context for the spectral comparison. Sensor P107 sits on the vertical rear face right under the highest deviation area, placing it directly below of the violent shear layer impingement zone. Meanwhile, sensors P105 and P106, located on the cavity side walls, register significantly lower fluctuation amplitudes; the standard deviation drops off sharply along the lateral boundaries compared to the intense, self-sustained pressure oscillations concentrated at the aft structures.

7. Summary and Outlook

This paper presents an experimental and high-fidelity numerical framework designed to isolate the effects of Reynolds number on transonic cavity aerodynamics. Testing in the Cryogenic Ludwieg-Tube Göttingen (KRG) reached within this test campaign unit Reynolds numbers up to 100 million per meter, enabling Reynolds sweeps at transonic Mach numbers up to 0.90. The experimental results demonstrate a highly synchronized global feedback loop, where the dynamic pressure data successfully capture clear resonant tracks corresponding to both the second and third Rossiter modes across the operational envelope. By systematically varying the stagnation temperature across the independent test cases, this approach separates the kinematic shifts associated with the speed of sound from the viscous boundary layer effects. While the global thermodynamic state determines the baseline dimensional frequency, the Reynolds number influences the underlying variations in the shear-layer dynamics. Because the present results characterize the initial, lower Reynolds number envelope of this research campaign, subsequent phases of the testing will evaluate whether these observed trends hold true at significantly higher Reynolds numbers closer to full-scale flight conditions.
The corresponding numerical investigations utilizing Improved Delayed Detached Eddy Simulations (IDDES) in the DLR TAU code complement these physical observations by resolving the complex, three-dimensional flow topology inside the cavity. The scale-resolving simulations successfully capture key features of the flow field, including the symmetric, counter-rotating streamwise vortices and the resulting surface footprint of intense pressure standard deviations concentrated along the aft wall.
Future research will extend this matrix to higher Reynolds numbers and test non-zero sideslip angles to evaluate asymmetric vortex shedding. Additionally, upcoming campaigns will evaluate the efficiency of passive flow control methodologies, specifically focusing on how upstream spoilers alter the shear layer characteristics and mitigate the resonant acoustics. To systematically isolate the role of the incoming boundary layer, the framework will leverage the model's geometric and structural flexibility. By systematically changing the height of the cavity, future work will map the precise influence of the incoming boundary layer thickness-to-cavity-height ratio. Furthermore, the incoming development length will be shortened using the alternative model leading-edge installation to directly manipulate the incoming boundary layer size before it undergoes separation at the cavity front lip. These validation data will help refine semi-empirical prediction tools and reduce risk in early design phases.

8. Contact Author Email Address

Mailto: andreas.goerttler@dlr.de

9. Copyright Statement

The authors confirm that they, and/or their company or organization, hold copyright on all of the original material included in this paper. The authors also confirm that they have obtained permission, from the copyright holder of any third party material included in this paper, to publish it as part of their paper. The authors confirm that they give permission, or have obtained permission from the copyright

holder of this paper, for the publication and distribution of this paper as part of the ICAS proceedings or as individual off-prints from the proceedings.

10. Acknowledgements

The authors gratefully acknowledges the scientific support and HPC resources provided by the German Aerospace Center (DLR). The HPC system CARO is partially funded by "Ministry of Science and Culture of Lower Saxony" and "Federal Ministry for Economic Affairs and Climate Action".

References

[1] Rossiter, J. E. Wind-tunnel experiments on the flow over rectangular cavities at subsonic and transonic speeds. *Aeronautical Research Council, Reports and Memoranda* No. 3438, 1964.

[2] Charwat, A. F., Dewey, Jr., C. F., Roos, J. N., and Hitz, J. A., "An investigation of separated flows, Part II," *Journal of Aerospace Sciences*, 28, 7, 1961. https://doi.org/10.2514/8.9099.

[3] Rockwell, D. and Naudascher, E. "Review – Self-Sustaining Oscillations of Flow Past Cavities," *ASME Journal of Fluids Engineering*, 100, 1978. https://doi.org/10.1115/1.3448624.

[4] Heller, H. H., Holmes, D. G. and Covert, E. E., "Flow-induced pressure oscillations in shallow cavities," *Journal of Sound and Vibration*, 18, 4, 1971. https://doi.org/10.1016/0022-460X(71)90105-2.

[5] Stallings, R. L., Jr. and Wilcox, F. J., "Experimental Cavity Pressure Distributions at Supersonic Speeds," *NASA TP-2683*, 1987.

[6] Plentovich, E. B., et al., "Experimental Cavity Pressure Measurements at Subsonic and Transonic Speeds," *NASA TP-3358*, 1993.

[7] Ahuja, K. K. and Mendoza, J. Effects of Cavity Dimensions, Boundary Layer, and Temperature on Cavity Noise With Emphasis on Benchmark Data To Validate Computational Aeroacoustic Codes *NASA Contractor Report 4653*, 1995.

[8] Ahlefeldt, T., Ernst, D., Goudarzi, A., Raumer, H.G., Spehr, C., "Aeroacoustic testing on a full aircraft model at high Reynolds numbers in the European Transonic Windtunnnel," *Journal of Sound and Vibration*, Vol. 566, No. 12 2023. https://doi.org/10.1016/j.jsv.2023.117926.

[9] Koch, S., Rosemann, H., Wagner, A., "The Cryogenic Ludwieg-Tube Göttingen (KRG) of the German Aerospace Center (DLR)," *Journal of large-scale research facilities*, Vol. 10, 2026 https://doi.org/10.17815/jlsrf-10-191

[10] Tracy, M. B. and Plentovich, E. B. "Characterization of Cavity Flow Fields Using Pressure Data Obtained in the Langley 0.3-Meter Transonic Cryogenic Tunnel," *NASA TM-4436*, 1993.

[11] Tracy, M. B., et al., "Effect of Sweep on Cavity Flow Fields at Subsonic and Transonic Speeds," *NASA/TM-2012-217577*, 2012.

[12] Lee, B. H. K., Orchard, D. M. and Tang, F. C., "Flow past a Yawed Rectangular Cavity in Transonic and Low Supersonic Flows," *Journal of Aircraft*, 46, 5, 2009. https://doi.org/10.2514/1.40729.

[13] Rajkumar, K., Tangermann, E. and Klein, M. Efficient Scale-Resolving Simulations of Open Cavity Flows for Straight and Sideslip Conditions. *Fluids* 2023, 8, 277.

[14] Bacci, D. and Saddington, A. J., "Angle of Attack Effects on the Induced Structural Loads of a Weapons Bay," *Aerotecnica Missili & Spazio*, 104, 2025. https://doi.org/10.1007/s42496-024-00240-6.

[15] Stallings, R. L., Jr., et al., "Measurements of store forces and moments and cavity pressures," *NASA TM-4611*, 1995.

[16] Tracy, M. B. and Plentovich, E. B., "Cavity Unsteady-Pressure Measurements at Subsonic and Transonic Speeds," *NASA TP-3669*, 1997.

[17] Kim, D. H., Choi, J. H, Kwan, O. J., "Detached eddy simulation of weapons bay flows and store separation," *Computers & Fluids*, Vol. 121, 2015. https://doi.org/10.1016/j.compfluid.2015.07.022.

[18] Barone, M. and Arunajatesan, S., "Pressure Loadings in a Rectangular Cavity with and Without a Captive Store," *Journal of Aircraft*, Vol. 53, 4, 2016. https://doi.org/10.2514/1.C033600.

[19] Ben-Gida, H., "Detached Eddy Simulations of Cavity-Store Interactions at Subsonic Turbulent Flow," *Aerospace*, 10, 935, 2023. https://doi.org/10.3390/aerospace10110935.

[20] Lawson, S. J. and Barakos, G. N., "Review of numerical simulations for high-speed, turbulent cavity flows," *Progress in Aerospace Sciences*, 47, 3, 2011. https://doi.org/10.1016/j.paerosci.2010.11.002.

[21] Menter, F. R., "Best Practice: Scale-Resolving Simulations in ANSYS CFD, Ver. 2.00," *ANSYS Inc*, 2015.

[22] Bacci, D., Saddington, A. J. and Ben-Gida, H., "RANS/LES and LBM/VLES Aero-Acoustic Analysis of Weapon Bays at Transonic Mach Number," *AIAA Paper 2025-3850*, 2025. https://doi.org/10.2514/6.2025-3850.

[23] Ferreira, C., "Gene expression programming: A new adaptive algorithm for solving problems," *Complex Systems*, 13, 2001.

[24] Rosemann, H. The Cryogenic Ludwieg-Tube Tunnel at Göttingen. *Special Course on Advances in Cryogenic Wind Tunnel Technology*, AGARD Rept. 812, 1997, pp. 8-1–8-13.

[25] Schwamborn, D., Gerhold, T., and Heinrich, R.: "The DLR TAU-Code: Recent Applications in Research and Industry," Proceedings of the European Conference on Computational Fluid Dynamics, Delft Univ. of Technology, Delft, The Netherlands, pp. 1–25, 2006

[26] Menter, F. R.: "Two-Equation Eddy-Viscosity Turbulence Models for Engineering Applications," AIAA Journal, Vol. 32, No. 8, pp. 1598–1605, 1994

[27] Probst, A., Löwe, J., Reuß, S., Knopp, T., Kessler, R., "Scale-Resolving Simulations with a Low-Dissipation Low-Dispersion Second-Order Scheme for Unstructured Flow Solvers", *AIAA Journal*, Vol. 54, 10, 2016, https://arc.aiaa.org/doi/10.2514/1.J054957

[28] BETA CAE Systems: "ANSA Pre Processor User Guide", https://www.beta-cae.com/ansa.htm [retrieved March 2025]